Quantification of the safety against groundwater ingress through longitudinal joints of segmental tunnel linings by means of convergences

Jiao-Long Zhang [a], Yong Yuan [a,*], Xian Liu [a], Herbert A. Mang [a,b], Bernhard L.A. Pichler [b,*]

[a] *College of Civil Engineering, Tongji University, Siping Road 1239, 200092 Shanghai, China*
[b] *Institute for Mechanics of Materials and Structures, TU Wien, Karlsplatz 13/202, 1040 Vienna, Austria*

ARTICLE INFO

ABSTRACT

Conventional inspection of groundwater leakage of segmental tunnel linings is a time-consuming task, while vertical and horizontal convergences are routinely measured in many tunnels. This provides the motivation to use convergences as input for the quantification of the safety against groundwater ingress through longitudinal joints of segmental tunnel linings. Measured convergences are translated into relative rotations at the joints. These rotations are then converted to changes of the compression of the gaskets. Combining these changes with results from testing of the gaskets allows for quantification of the remaining sealing pressure. The safety against groundwater ingress is quantified by means of the ratio between the remaining sealing pressure and the groundwater pressure. To ensure efficient application in tunnel engineering, closed-form equations are provided in the analysis whenever possible. The method is validated by comparing model predictions with inspection data of the segmental lining of Metro Line 7, in Shanghai. Finally, the effectiveness of two sets of gaskets per longitudinal joint is assessed. It is concluded that a symmetric arrangement of two pairs of gaskets, one close to the outer edge and the other close to the inner edge of the joint, significantly increases the water tightness as long as the sealing of the bolt channels can be guaranteed. Otherwise, an eccentric arrangement of two pairs of gaskets, both close to the outer edge, is a good option.

1. Introduction

Groundwater leakage and ovalization of initially circular segmental linings are threats to the serviceability of tunnels (Yuan et al., 2012). As regards related structural monitoring, inspection methods must comply with two main requirements: (i) the monitoring data must be of suitable quality such as to allow for a quantitative assessment of the serviceability of the tunnels and (ii) the inspection methods shall affect the regular operation of the tunnels as little as possible.

The ovalization of tunnel linings is usually monitored by means of measuring convergences, representing changes of the diameter of initially circular tunnel linings. A convergence-related serviceability limit state is reached as soon as the largest convergence reaches or exceeds a certain fraction of the initial diameter of the lining, e.g. 2% according to the Chinese code of practice (DG/TJ08-2123-2013, 2013). Convergences are usually measured in the vertical and the horizontal direction. Manual measurements (Li et al., 2017) are time consuming and the regular operation of the tunnel must be interrupted during inspection. In order to improve this situation, laser scanning technology, installed on a rail-bound vehicle, was used for tunnel inspections (Nuttens et al., 2014; Xie and Lu, 2017). Displacements of many points of the lining are automatically acquired while the vehicle moves through the tunnel (Cui et al., 2019). This reduces the negative effect of the inspection of the tunnels on their operation to a tolerable minimum. The collected data are postprocessed off-site. It is popular to represent the deformed state of a tunnel cross-section by an ellipse which approximates the deformation measurements in the best-possible fashion (Walton et al., 2014). A more advanced approach, accounting for discontinuities at the longitudinal joints, connecting neighboring segments of a tunnel ring, consists of representing the deformed configuration of every single tubbing by a specific segment of an ellipse (Xu et al., 2022). The convergences in the vertical and the horizontal direction are eventually determined from the deformed configuration which was back-analyzed from the monitoring data. Herein, convergences, taken from (Ai and Yuan, 2019), will be used to assess the safety against groundwater ingress through longitudinal joints.

Groundwater leakage increases the likeliness of deterioration of both the lining itself and the electrical equipment required for tunnel operation (Gong et al., 2019). Groundwater-leakage-related serviceability limit states are usually defined by limiting the average daily volume of groundwater running into the tunnel per $100\,\text{m}^2$ of its inner

---

surface. According to the Chinese code of practice (T/CSPSTC 43-2019, 2019), related threshold values depend on the importance grade of the tunnel. Groundwater leakage is usually monitored by means of visual inspection which is expensive in terms of both time and manpower. In order to improve this situation, artificial intelligence concepts were developed to detect groundwater leakage (Huang et al., 2018; Attard et al., 2018; Huang et al., 2021). One promising approach refers to detecting sites of groundwater ingress by means of analyzing gray-scale images produced from 3D laser scanning data (Yi et al., 2019; Huang et al., 2020). Together with his colleagues, the second author of the present paper developed a machine learning approach, based on photos taken by charge-coupled device (CCD) cameras (Ai et al., 2016). These photos allow for measuring the convergences of tunnel rings and for detecting groundwater leakage sites simultaneously (Ai and Yuan, 2019). The inspection of 13 segmental linings of tunnels crossing the Huangpu River in Shanghai below the riverbed has shown that groundwater leakage mainly occurs at the joints of segmental tunnel linings (Wu et al., 2014).

The following two points provide the motivation for the present analysis.

- Anticipatory planning of maintenance and repair of tunnels would benefit significantly from the possibility to quantify the safety against groundwater ingress into the tunnel *before* a leakage problem is encountered. Provided that a suitable safety factor could be defined and quantified, its evolution could be monitored. Trends derived from monitoring data could be used for predicting the remaining time before the occurrence of significant groundwater leakage.
- Significant ingress of groundwater can be identified rather easily by monitoring the amount of water running through the drainage system of the tunnel. However, localization of the actual sites through which the groundwater runs into the tunnel is a much more challenging task. Provided that the safety against groundwater ingress into the tunnel could be quantified, the search for leakage sites could be focused on stretches of the tunnel where the likeliness of groundwater ingress is known to be specifically high.

Notably, a statistical analysis of monitoring data, obtained from inspection of 360 segmental rings of a damaged metro tunnel in Shanghai, indicated a correlation between groundwater ingress through longitudinal joints and the convergences (Huang et al., 2017). This is setting the scene for the present paper.

The objective of the present paper is to check whether or not it is possible to quantify the safety against groundwater ingress through longitudinal joints of a segmental tunnel lining by means of a multiscale engineering mechanics approach. It uses convergences, measured in the vertical and the horizontal direction, as input. The analysis starts at the largest scale, i.e. at the one of the tunnel rings, and then proceeds to ever smaller scales, namely, first to the joints and then to the gaskets. This two-step approach will be explained in the following:

1. In the first step, relative rotations at the joints are quantified from convergences measured in the vertical and the horizontal direction. The rationale behind this step is that (i) the convergences of segmental tunnel rings are governed by rigid-body displacements of the tubbings (Zhang et al., 2017, 2019a), and (ii) these displacements go along with relative rotations at the longitudinal joints (Blom, 2002; El Naggar and Hinchberger, 2008). The transformation of two measured convergences into six relative rotations at the joints follows research by Jiang et al. (2021) and Zhang et al. (2022a). In more detail, the rigid-body displacements of the investigated tunnel rings, consisting of six tubbings, are described as a linear combination of three modes of rigid-body displacements (Jiang et al., 2021). Each one of them represents a specific set of six relative rotations at the joints.

The components of these modes, i.e. the scalar factors by which these modes are multiplied, are obtained as the solution of an optimization problem, characterized by the use of convergences measured in the vertical and the horizontal direction as input (Zhang et al., 2022a).

2. The second step refers to the conversion of the relative rotations at the joints into changes of the sealing pressure of the gaskets. The rationale behind this step is that (i) gaskets are compressed in the intended circular initial configuration of the tunnel ring, resulting in a specific initial sealing pressure (Gong et al., 2022), and (ii) relative rotations at the joints increase or decrease this initial compression, resulting in an increase or decrease of the sealing pressure (Zhang et al., 2022b; Meng et al., 2023). Relative rotations at the joints are converted into changes of the shortening of the gaskets by means of a newly proposed kinematic analysis. Changes of the sealing pressure are quantified with the help of changes of the shortening of the gaskets, using results from direct compression tests of the gaskets.

Finally, an index for quantification of the safety against groundwater ingress is introduced. It is equal to the ratio between the sealing pressure in the deformed configuration and the groundwater pressure. This is useful for closed-base gaskets (Shalabi et al., 2016). The described method is used to predict the relation between the convergences and the safety against groundwater ingress into the segmental tunnel lining of Metro Line 7, in Shanghai. The predictions will be validated based on measured convergences of tunnel rings through which water was actually running into the tunnel (Ai and Yuan, 2019).

Notably, state-of-the-art approaches regarding the assessment of the sealing performance of gasketed joints combine advanced laboratory testing with numerical simulations of the interaction between the gaskets and the segments (Gong et al., 2022; Zhang et al., 2022b; Meng et al., 2023). These approaches are directly applicable provided that the dislocations at the joints, both in the tangential and the radial direction, and the relative rotations are known. However, on site quantification of joint deformations remains a challenging task, no matter whether performed by manual measurements or laser scanning (Xu et al., 2019). The novelty of the present paper consists in the development of a concept that allows for relating an index that quantifies the safety against groundwater ingress to measured convergences. Thereby, closed-form equations are provided whenever possible. They ensure efficient numerical applicability in tunnel engineering.

The paper is organized as follows. Section 2 contains fundamentals required for transforming convergences into relative rotations at the joints. Section 3 is devoted to converting the relative rotations at the joints first into changes of the shortening of the gaskets, then into the remaining gasket-to-gasket contact pressure, and finally into the aforementioned index for determination of the safety against water ingress. In Section 4, the described method will be applied to Metro Line 7 in Shanghai. In Section 5, the developed method will be used to assess the effectiveness of placing two sets of gaskets at each longitudinal joint. Section 6 contains the conclusions drawn from the presented study.

2. Fundamentals: quantification of relative rotations at longitudinal joints from known convergences (Zhang et al., 2022a)

Herein a segmental ring consisting of six tubbings, as are used for the linings of metro tunnels in Shanghai, is considered, see Fig. 1(a). The radius of the axis of the ring, R, amounts to 2.925 m. The angular coordinate, φ, is measured counterclockwise from the crown. The joints are located at

$$\varphi_1 = 8°, \quad \varphi_2 = 73°, \quad \varphi_3 = 138°, \quad \varphi_4 = 222°, \quad \varphi_5 = 287°, \quad \varphi_6 = 352°.$$
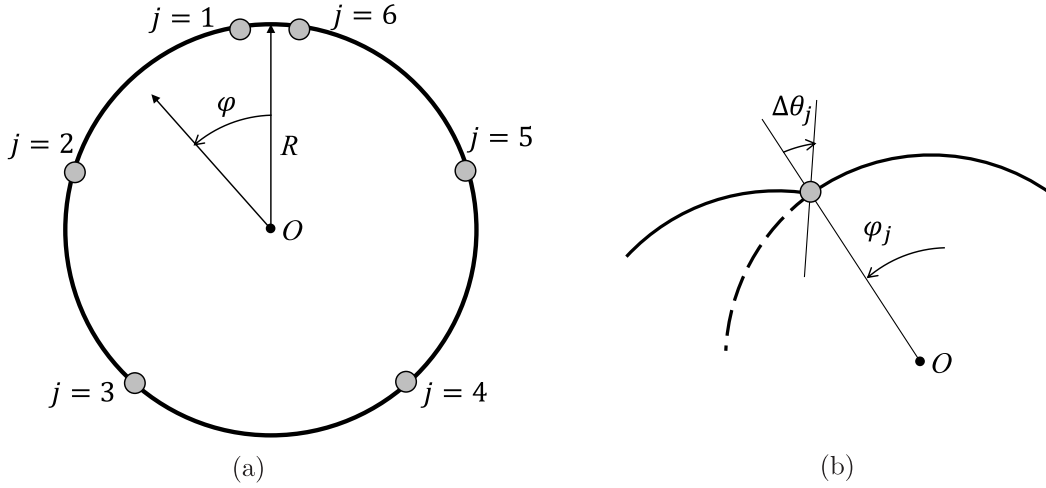(1)

Fig. 1. Tubbing ring used for the segmental linings of metro tunnels in Shanghai: (a) arrangement of the segments, numbering of the joints, radius of the axis of the ring, and angular coordinate, (b) relative rotation at the jth joint, $\Delta\theta_j$.

Relative rotations at the six joints, resulting in rigid-body displacements of the tubbings, satisfy the conditions (A.4)–(A.6), as explained in Appendix A. There are infinitely many solutions for the six relative rotations satisfying these conditions. All of these solutions can be mathematically expressed in the form of a linear combination of three fundamental solutions. Zhang et al. (2019a) introduced a fundamental solution, referring to a symmetric mode of rigid-body displacements, see Fig. 2(a). Jiang et al. (2021) introduced two fundamental solutions, referring to two antisymmetric modes of rigid-body displacements, Figs. 2(b) and (c). These three solutions form a basis of the solutions for the six relative rotations satisfying Eqs. (A.4)–(A.6). After their orthonormalization, the corresponding values of these rotations at the joints, see also Fig. 1(b), can be expressed as (Jiang et al., 2021)

$$
\begin{bmatrix} \Delta\theta_1 \\ \Delta\theta_2 \\ \Delta\theta_3 \\ \Delta\theta_4 \\ \Delta\theta_5 \\ \Delta\theta_6 \end{bmatrix} = \underbrace{\begin{bmatrix} +0.3427 & +0.6923 & -0.1171 \\ -0.5737 & \pm0.0000 & +0.4111 \\ +0.2310 & -0.1440 & -0.5632 \\ +0.2310 & +0.1440 & +0.5632 \\ -0.5737 & \mp0.0000 & -0.4111 \\ +0.3427 & -0.6923 & +0.1171 \end{bmatrix}}_{\boldsymbol{A}} \cdot \underbrace{\begin{bmatrix} \beta_1 \\ \beta_2 \\ \beta_3 \end{bmatrix}}_{\boldsymbol{\beta}},
\tag{2}
$$

where the three columns of the matrix $\boldsymbol{A}$ refers to the orthonormalized basis, see details in (Jiang et al., 2021; Zhang et al., 2022a). Thus,

$$
\sum_{i=1}^{6} A_{ij}\,A_{ik} = \delta_{jk}, \quad \forall j,k \in \{1\,;\,2\,;\,3\},
\tag{3}
$$

where A_{ij} denotes the component of $\boldsymbol{A}$ in the ith row and the jth column, and where δ_{jk} denotes the Kronecker delta. It is equal to 1 for $j = k$ and to 0 otherwise.

The first column of the matrix $\boldsymbol{A}$ in Eq. (2) refers to the symmetric mode of rigid-body displacements illustrated in Fig. 2(a). The remaining two columns refer to the two antisymmetric modes of rigid-body displacements illustrated in Figs. 2(b) and (c). β_1, β_2, and β_3 denote scalar components of the three orthonormalized modes of rigid-body displacements. The related convergence C at $\varphi = \psi_k$ in the direction of

the diameter at that angle can be expressed as (Zhang et al., 2022a)

$$
\begin{aligned}
C(\psi_k;\beta_1,\beta_2,\beta_3) = &\left\{ \left[2R + \sum_{j=1}^{6} R\left(A_{j,1}\,\beta_1 + A_{j,2}\,\beta_2 + A_{j,3}\,\beta_3\right) \times \right. \right. \\
&\left. \left\{ \sin(\psi_k - \varphi_j)H(\psi_k - \varphi_j) + \sin(\psi_k + \pi - \varphi_j)H(\psi_k + \pi - \varphi_j) \right\} \right]^2 + \\
&\left[\sum_{j=1}^{6} R\left(A_{j,1}\,\beta_1 + A_{j,2}\,\beta_2 + A_{j,3}\,\beta_3\right) \left\{ \left[1 - \cos(\psi_k - \varphi_j)\right]H(\psi_k - \varphi_j) + \right. \right. \\
&\left. \left. \left[1 - \cos(\psi_k + \pi - \varphi_j)\right]H(\psi_k + \pi - \varphi_j) \right\}\right]^2 \right\}^{\frac{1}{2}} - 2R.
\end{aligned}
\tag{4}
$$

Introducing "1" and "2" as indices for the horizontal and the vertical direction, respectively, the corresponding angles ψ_k read as:

$$
\psi_1 = 90°,
\tag{5}
$$
$$
\psi_2 = 180°.
\tag{6}
$$

β_1, β_2, and β_3 are identified from the measured values of horizontal and vertical convergences, denoted by $C^{mea}(\psi_1)$ and $C^{mea}(\psi_2)$, respectively, by means of the following two-step identification procedure (Zhang et al., 2022a):

Step 1: β_2 and β_3 are set equal to zero. The value of β_1 is optimized by means of minimizing the root mean square error between measured and modeled convergences:

$$
RMS(\beta_1) = \sqrt{\frac{1}{2}\sum_{k=1}^{2}\left[C^{mea}(\psi_k) - C(\psi_k;\beta_1,\beta_2 = 0,\beta_3 = 0)\right]^2} \to \min.
\tag{7}
$$

Step 2: β_1 is kept constant at the optimal value β_1^{opt} determined in Step 1. The values of β_2 and β_3 are optimized by means of reducing the root mean square error between measured and modeled convergences to zero:

$$
RMS(\beta_2,\beta_3) = \sqrt{\frac{1}{2}\sum_{k=1}^{2}\left[C^{mea}(\psi_k) - C(\psi_k;\beta_1 = \beta_1^{opt},\beta_2,\beta_3)\right]^2} \to 0.
\tag{8}
$$

$$\beta_1 > 0, \ \beta_2 = \beta_3 = 0 \qquad \beta_2 > 0, \ \beta_1 = \beta_3 = 0 \qquad \beta_3 > 0, \ \beta_1 = \beta_2 = 0$$
$$\text{(a)} \qquad\qquad\qquad \text{(b)} \qquad\qquad\qquad \text{(c)}$$
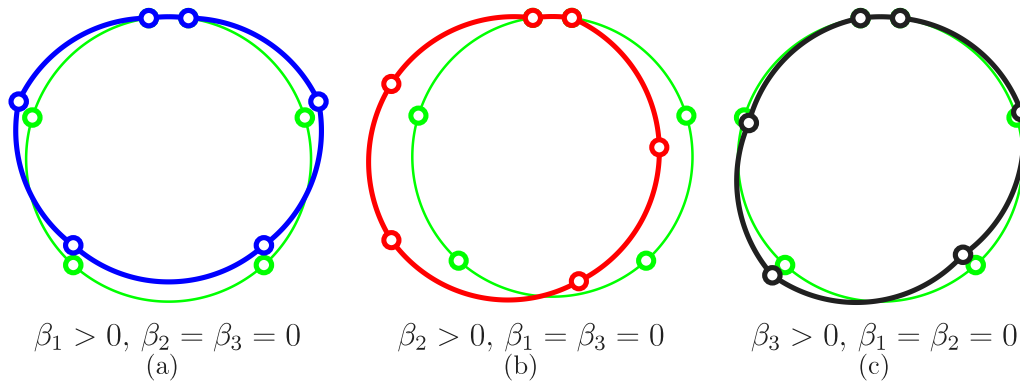
Fig. 2. Three orthonormalized modes of rigid-body displacements of the tubbings: (a) symmetric mode, (b) first antisymmetric mode, (c) second antisymmetric mode; the circles refer to the joints; after (Jiang et al., 2021).

Table 1
Numerical values of the geometric dimensions labeled in Figs. 3(a), 5, 6, and 16.

$L_1 = 210\,\text{mm}$	$L_2 = 35\,\text{mm}$	$L_3 = 25\,\text{mm}$	$L_4 = 42\,\text{mm}$	$L_5 = 36\,\text{mm}$
$L_6 = 4\,\text{mm}$	$L_7 = 4\,\text{mm}$	$L_8 = 8\,\text{mm}$	$L_9 = 150\,\text{mm}$	$h = 350\,\text{mm}$

Table 2
Numerical values of calibration parameters k_1, k_2, and k_3, the constants d_2 and d_3, the interval boundaries Δl_{t1} and Δl_{t2}, introduced in Eqs. (9), as well as initial shortening of the gaskets Δl_{ini} according to Eq. (12); the values of d_2 and d_3 were quantified based on Eqs. (10) and (11).

$k_1 = 0.0919\,\text{MPa/mm}$		$\Delta l_{t1} = 3.5\,\text{mm}$
$k_2 = 0.5014/\text{mm}$	$d_2 = -2.8892$	$\Delta l_{t2} = 5.4\,\text{mm}$
$k_3 = 0.9834/\text{mm}$	$d_3 = -5.4920$	$\Delta l_{ini} = 6.0\,\text{mm}$

Once β_1^{opt}, β_2^{opt}, and β_3^{opt} are identified, they are inserted into Eq. (2) in order to quantify the corresponding values of the relative rotations at the joints. The latter are the basis for the assessment of the safety against leakage at the joints.

3. Assessment of the safety against leakage at longitudinal joints based on known relative rotations

Gaskets made of an Ethylene–Propylene–Diene Monomer (EPDM) are used to render longitudinal joints of segmental linings of metro tunnels in Shanghai groundwater-proof, see Fig. 3(a) and Table 1. The gaskets are glued into grooves of the prefabricated reinforced-concrete tubbings. During installation of a tubbing ring, two gaskets are pressed at each other at each joint. As long as the resulting contact pressure σ is larger than the hydraulic stress resulting from the external groundwater pressure p_w,[1] the gaskets prevent the groundwater from running into the tunnel, see Fig. 3(b). The relation between the contact pressure σ and the shortening Δl imposed on a gasket was determined experimentally by Shen (2012), see Fig. 4. The measured data are described by means of the following function:

$$\sigma = \begin{cases} k_1 \, \Delta l \ \dots\dots\dots\dots\dots\dots\dots\dots \ 0 \le \Delta l \le \Delta l_{t1}, \\ 1\,\text{MPa} \times \exp\!\left(k_2 \, \Delta l + d_2\right) \dots \ \Delta l_{t1} \le \Delta l \le \Delta l_{t2}, \\ 1\,\text{MPa} \times \exp\!\left(k_3 \, \Delta l + d_3\right) \dots \ \Delta l_{t2} \le \Delta l, \end{cases} \tag{9}$$

where k_1, k_2, and k_3 are calibration parameters, see Table 2. The constants d_2 and d_3 are related to k_1, k_2, and k_3 such as to ensure continuity at the boundaries between the intervals given in Eq. (9):

$$d_2 = \ln\!\left(\frac{k_1 \, \Delta l_{t1}}{1\,\text{MPa}}\right) - k_2 \, \Delta l_{t1}, \tag{10}$$

$$d_3 = d_2 + (k_2 - k_3) \, \Delta l_{t2}. \tag{11}$$

The three lines in Eq. (9) refer to three different intervals of Δl. The interval boundaries are denoted as Δl_{t1} and Δl_{t2}. Numerical values of the boundaries between these intervals are given in Table 2.

The height l_0 of the undeformed trapezoidal gaskets, measured in circumferential direction of the tunnel ring, amounts to 16 mm, see the insert in Fig. 3(a). Provided that two neighboring tubbings are installed

---

[1] Compressive stresses (= pressures) are introduced with a positive mathematical sign, tensile stresses with a negative sign.

as illustrated in Fig. 3(a), the height of each one of the two trapezoidal gaskets is reduced by

$$\Delta l_{ini} = 6\,\text{mm} \tag{12}$$

to 10 mm. This "initial" shortening activates a contact pressure amounting to $1.50\,\text{MPa}$, see Fig. 4.

The contact pressure σ changes as a function of the relative rotations at the joints. A positive relative rotation opens the joint at the inner side, see Fig. 5, while a negative relative rotation opens it at the outer side, see Fig. 6.

The relation between positive and negative relative rotations at the joints, on the one hand, and the shortening of the gaskets and their contact pressure, on the other hand, as well as the associated safety against leakage will be dealt with in the remainder of this paper. In order to keep the corresponding mathematical description reasonably simple, linearized rigid body kinematics of reinforced-concrete tubbings will be assumed.

3.1. Changes of the shortening of the gaskets resulting from relative rotations at the longitudinal joints

As regards monotonously increasing *positive* relative rotations, the analysis consists of two stages. In Stage 1, the center of the relative rotation is point B, see Fig. 5(a). In Stage 2, it is point A, see Fig. 5(b). The transition from Stage 1 to Stage 2 takes place as soon as the relative rotation around point B closes the initial gap between points A_l and A_r in Fig. 3(a). The corresponding relative rotation is equal to the initial tangential distance between points A_l and A_r, see L_6 in Fig. 3(a), divided by their radial distance from point B, see $L_4 + L_5$ in Fig. 3(a):

$$\Delta\theta_{1\to2} = \frac{L_6}{L_4 + L_5}. \tag{13}$$

Water ingress resulting from the increasing positive relative rotation will take place as soon as the compressive stress at the *outer* edges of the gaskets (= the upper edges in Fig. 5) has decreased to the groundwater pressure. Therefore, the following analysis is focused on the outer edges of the gaskets.

Positive relative rotations, Stage 1: Provided that the relative rotation increases from zero to $\Delta\theta_{1\to2}$, the shortening of both
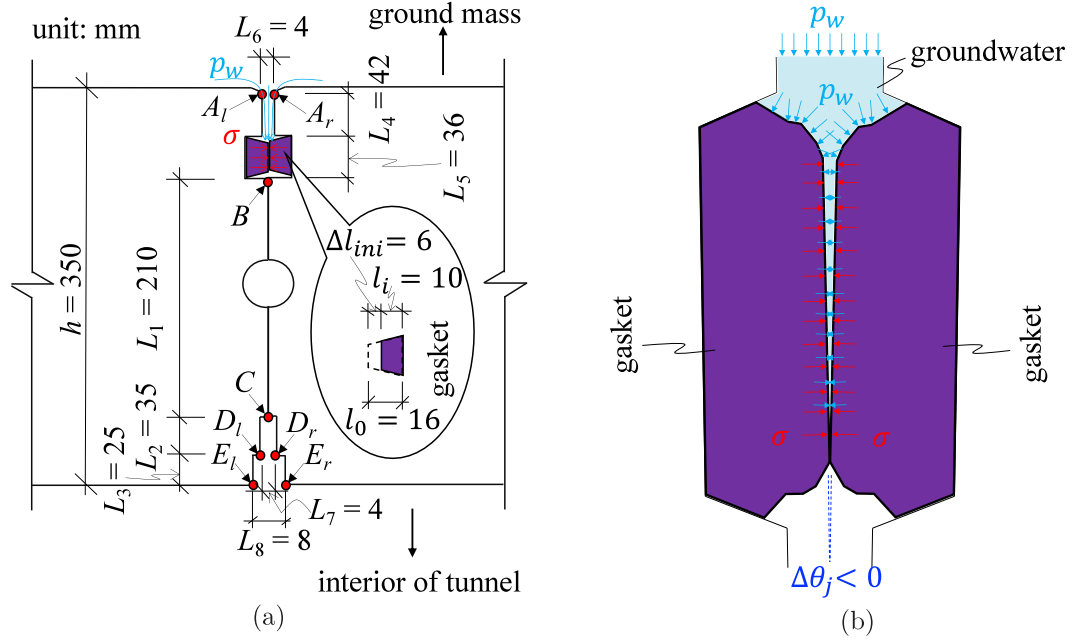
Fig. 3. (a) Geometric properties of a longitudinal joint between neighboring tubbings used for segmental linings of metro tunnels in Shanghai and (b) sketch of the forces acting on the gaskets in case of $\Delta\theta_j < 0$; note that the magnification factor in subfigure (b) is 10 compared to that in subfigure (a) and that the scales in the radial and the tangential direction are different in order to increase the comprehensibility of the figure, see also Table 1.
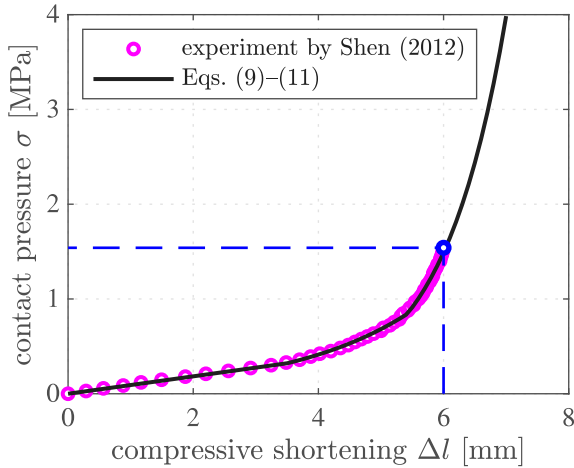

Fig. 4. Relation between the contact pressure and the shortening of the EPDM gaskets used in metro tunnels in Shanghai: the pink circles mark test results by Shen (2012); the solid line refers to Eqs. (9)–(11), and the dashed lines refer to the shortening which results from the installation of a tunnel ring, see Eq. (12), as well as to the corresponding contact pressure which amounts to 1.50 MPa.

gaskets at their outer edges increases by an amount which is equal to the relative rotation $\Delta\theta$ multiplied by the radial distance of the outer edge of the gaskets from point B, see L_5 in Fig. 5(a). Dividing this product by 2 in order to compute the shortening of one gasket and adding the result to the initial shortening, delivers

$$\Delta l_1(\Delta\theta > 0) = \Delta l_{ini} + \frac{L_5}{2}\Delta\theta, \qquad 0 \leq \Delta\theta \leq \frac{L_6}{L_4 + L_5}, \qquad (14)$$

see also the red line in Fig. 7. The shortening at the end of Stage 1 (= transition to Stage 2) follows from setting $\Delta\theta$ in Eq. (14) equal to $\Delta\theta_{1\rightarrow2}$:

$$\Delta l_{1\rightarrow2} = \Delta l_{ini} + \frac{L_5}{2}\Delta\theta_{1\rightarrow2}. \qquad (15)$$

Positive relative rotations, Stage 2: With increasing relative rotation angle, the shortening of both gaskets at their outer edges decreases by an amount equal to $\Delta\theta - \Delta\theta_{1\rightarrow2}$ multiplied by the radial distance of the outer edge of the gaskets from point A, see L_4 in Fig. 5(b). Dividing this product by 2 in order to compute the shortening of one gasket at its outer edge and adding the result to $\Delta l_{1\rightarrow2}$ according to Eq. (15), yields the shortening in Stage 2 as

$$\Delta l_2(\Delta\theta > 0) = \Delta l_{ini} + \frac{L_5}{2}\Delta\theta_{1\rightarrow2} - \frac{(\Delta\theta - \Delta\theta_{1\rightarrow2})L_4}{2}. \qquad (16)$$

Collection of terms proportional to $\Delta\theta_{1\rightarrow2}$ in Eq. (16), insertion of Eq. (13) into the resulting expression, and simplification of the result yields:

$$\Delta l_2(\Delta\theta > 0) = \Delta l_{ini} + \frac{L_6}{2} - \frac{L_4}{2}\Delta\theta, \qquad \frac{L_6}{L_4 + L_5} < \Delta\theta \leq \frac{2\Delta l_{ini} + L_6}{L_4}, \qquad (17)$$

see also the blue line in Fig. 7. Notably, $(2\Delta l_{ini} + L_6)/L_4$ in Eq. (17) is equal to the relative rotation at the end of Stage 2, at which the two gaskets separate. It is obtained by setting $\Delta l_2(\Delta\theta > 0)$ in Eq. (17) equal to 0 and solving the resulting expression for $\Delta\theta$.

As regards monotonously increasing *negative* relative rotations, point C is the center of rotation, see Fig. 6. Ingress of groundwater will take place as soon as the compressive stress at the *inner* edges of the gaskets (= the lower edges in Fig. 6) has decreased to the groundwater pressure. Therefore, the following analysis is focused on the inner edges of the gaskets.

The shortening of each one of the two gaskets at their inner edge is equal to the initial shortening, Δl_{ini}, plus one half of the relative rotation $\Delta\theta$ multiplied by the radial distance of the inner edges of the gaskets from the center of rotation (= point C), see L_1 in Fig. 6,

$$\Delta l(\Delta\theta < 0) = \Delta l_{ini} + \frac{L_1}{2}\Delta\theta, \qquad -\frac{2\Delta l_{ini}}{L_1} < \Delta\theta \leq 0. \qquad (18)$$

see also the black line in Fig. 7. Notably, $-2\Delta l_{ini}/L_1$ in Eq. (18) is equal to the relative rotation at which the two gaskets separate. It is
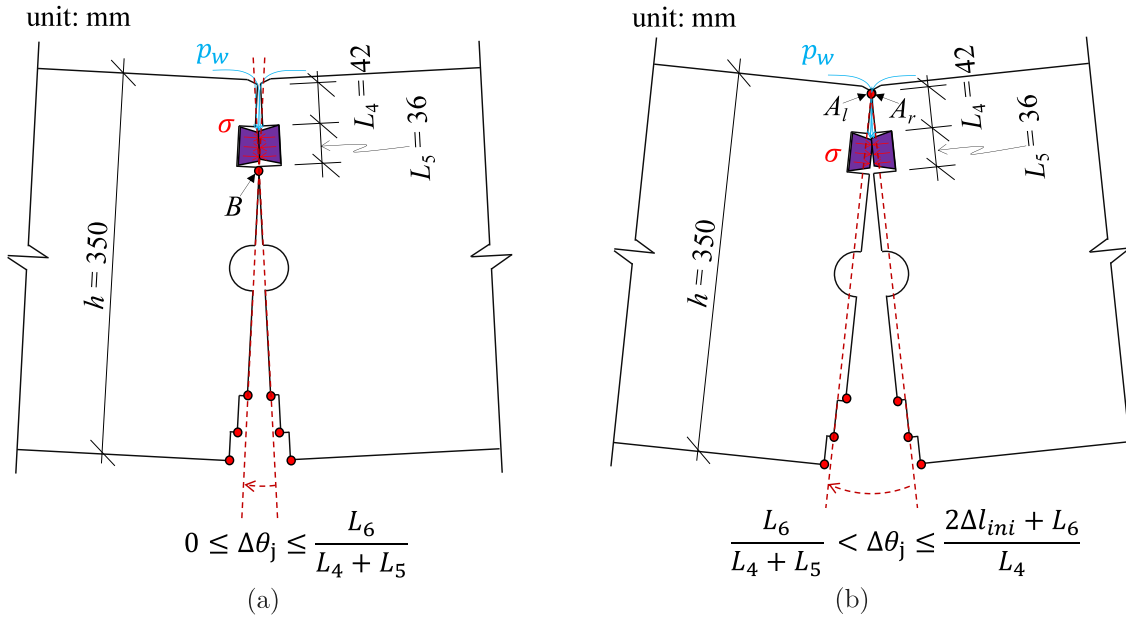
Fig. 5. Rigid-body displacements associated with a positive relative rotation at a longitudinal joint: (a) Stage 1: the center of rotation is located at point B, (b) Stage 2: the center of rotation is located at point A; for the derivation of the rotation ranges see Eqs. (13)–(17); note that the scales in the radial and the tangential direction are different in order to increase the comprehensibility of the figure.

obtained by setting $\Delta l (\Delta \theta < 0)$ in Eq. (18) equal to 0 and solving the resulting expression for $\Delta \theta$. In order to prove that the rotation center remains at point C rather than changing to point D, it is checked that the initial gap between points D_l and D_r in Fig. 3(a) has not closed. In mathematical terms, the product of the absolute value of the rotation, $2 \Delta l_{ini} / L_1$, multiplied by the radial distance of the points D_r and D_l from the center of rotation (= point C), see L_2 in Fig. 6, must be smaller than the initial tangential distance between D_r and D_l, see L_7 in Fig. 3(a):

$$\frac{2 \Delta l_{ini}}{L_1} L_2 < L_7 . \tag{19}$$

Insertion of numerical values from Table 1 into the inequality (19) delivers a true answer. This proves that point C remains the center of rotation, because the points D_r and D_l remain separated. It demonstrates the validity of Eq. (18).

3.2. Changes of the contact pressure between the gaskets resulting from relative rotations at the longitudinal joints

Closed-form relations between the contact pressure and the relative rotation are obtained by inserting the expressions for the shortening according to Eqs. (14), (17), and (18), see also Fig. 7, into Eqs. (9), see also Fig. 4, and considering the numerical values listed in Tables 1 and 2. The obtained relations read as

$$\sigma = \begin{cases} k_1 \left[\Delta l_{ini} + \frac{L_1}{2} \Delta \theta \right] & \cdots\cdots\cdots\cdots\cdots\cdots \quad \Delta \theta_{n3} \leq \Delta \theta \leq \Delta \theta_{n2} , \\ 1\,\text{MPa} \times \exp\!\left(k_2 \left[\Delta l_{ini} + \frac{L_1}{2} \Delta \theta \right] + d_2 \right) & \cdots\cdots \quad \Delta \theta_{n2} \leq \Delta \theta \leq \Delta \theta_{n1} , \\ 1\,\text{MPa} \times \exp\!\left(k_3 \left[\Delta l_{ini} + \frac{L_1}{2} \Delta \theta \right] + d_3 \right) & \cdots\cdots\cdots \quad \Delta \theta_{n1} \leq \Delta \theta \leq 0 , \\ 1\,\text{MPa} \times \exp\!\left(k_3 \left[\Delta l_{ini} + \frac{L_5}{2} \Delta \theta \right] + d_3 \right) & \cdots\cdots\cdots \quad 0 \leq \Delta \theta \leq \Delta \theta_{p1} , \\ 1\,\text{MPa} \times \exp\!\left(k_3 \left[\Delta l_{ini} + \frac{L_6}{2} - \frac{L_4}{2} \Delta \theta \right] + d_3 \right) & \cdots \quad \Delta \theta_{p1} \leq \Delta \theta \leq \Delta \theta_{p2} , \\ 1\,\text{MPa} \times \exp\!\left(k_2 \left[\Delta l_{ini} + \frac{L_6}{2} - \frac{L_4}{2} \Delta \theta \right] + d_2 \right) & \cdots \quad \Delta \theta_{p2} \leq \Delta \theta \leq \Delta \theta_{p3} , \\ k_1 \left[\Delta l_{ini} + \frac{L_6}{2} - \frac{L_4}{2} \Delta \theta \right] & \cdots\cdots\cdots\cdots\cdots \quad \Delta \theta_{p3} \leq \Delta \theta \leq \Delta \theta_{p4} . \end{cases} \tag{20}$$

with

$$\begin{aligned} \Delta \theta_{n3} &= -\frac{2 \Delta l_{ini}}{L_1} , & \Delta \theta_{p1} &= \frac{L_6}{L_4 + L_5} , \\ \Delta \theta_{n2} &= \frac{2 (\Delta l_{t1} - \Delta l_{ini})}{L_1} , & \Delta \theta_{p2} &= \left(\Delta l_{ini} + \frac{L_6}{2} - \Delta l_{t2} \right) \frac{2}{L_4} , \\ \Delta \theta_{n1} &= \frac{2 (\Delta l_{t2} - \Delta l_{ini})}{L_1} , & \Delta \theta_{p3} &= \left(\Delta l_{ini} + \frac{L_6}{2} - \Delta l_{t1} \right) \frac{2}{L_4} , \\ & & \Delta \theta_{p4} &= \left(\Delta l_{ini} + \frac{L_6}{2} \right) \frac{2}{L_4} . \end{aligned} \tag{21}$$

see also Fig. 8. In the initial configuration of a tubbing ring, all relative rotations at the joints are equal to zero, and the contact pressure between the gaskets amounts to 1.50 MPa. Provided that a *positive* relative rotation develops at a joint (= opening at the inside), the contact pressure increases until points A_l and A_r get in contact. Thereafter, a continued increase of the relative rotation results in a monotonously decreasing contact pressure. The latter vanishes at

$$\Delta \theta = \frac{2}{L_4} \left(\Delta l_{ini} + \frac{L_6}{2} \right) = +0.381 \, \text{rad} , \tag{22}$$

as obtained from setting σ in Eq. (20) equal to zero, solving the last line of this equation for $\Delta \theta$, and inserting numerical values from Tables 1 and 2 into the resulting expression. Provided that a *negative* relative rotation develops at a joint (= opening at the outside), the contact pressure decreases monotonously and vanishes at

$$\Delta \theta = -\frac{2 \Delta l_{ini}}{L_1} = -0.057 \, \text{rad} , \tag{23}$$

as obtained from setting σ in Eq. (20) equal to zero, solving the first line of this equation for $\Delta \theta$, and inserting numerical values from Tables 1 and 2 into the resulting expression. Fig. 8 underlines that negative relative rotations are more problematic for joints than positive ones. A negative relative rotation results in a larger change of shortening of the gaskets than a positive relative rotation of the same absolute value, see Figs. 5 and 6, because the gaskets are closer to the groundmass than to the interior of the tunnel.

3.3. Assessment of the safety against leakage based on the contact pressure between the gaskets and the groundwater pressure

Introducing the groundwater pressure in Fig. 8, see the magenta dashed graph parallel to the abscissa, yields two points of intersection
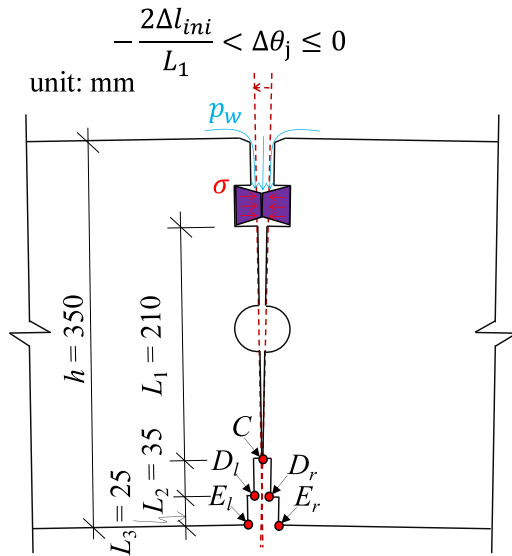
$$-\frac{2\Delta l_{ini}}{L_1} < \Delta\theta_{\mathrm{j}} \leq 0$$

unit: mm

Fig. 6. Rigid-body displacements associated with a negative relative rotation at a longitudinal joint: the center of rotation is located at point C; note that the scales in the radial and the tangential direction are different in order to increase the comprehensibility of the figure.
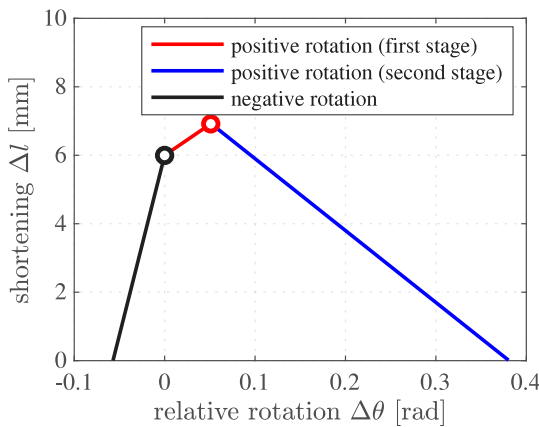

Fig. 7. Shortening of the gaskets as a function of the relative rotation according to Eq. (14), see the red line, Eq. (17), see the blue line, and Eq. (18), see the black line. (For interpretation of the references to color in this figure legend, the reader is referred to the web version of this article.)

Fig. 8. Contact pressure between the gaskets as a function of the relative rotation according to Eqs. (20) and (21) with numerical values taken from Tables 1 and 2. (For interpretation of the references to color in this figure legend, the reader is referred to the web version of this article.)

Fig. 9. Relative rotations at which the groundwater-ingress limit state is reached at a joint as a function of the groundwater pressure p_w acting on the gaskets; the two graphs refer to situations for which the contact pressure between the gaskets is equal to the groundwater pressure ($\sigma = p_w$), i.e. to $\xi = 1$, see Eq. (24).

with the curves relating the contact pressure between the gaskets to the relative rotations. These two points refer to groundwater-ingress limit states. In between them, the joint will be leakproof, see the purple area in Fig. 8.

A joint-related factor quantifying the safety against groundwater ingress is introduced as the ratio between the remaining sealing pressure σ and the groundwater pressure p_w:

$$\xi = \frac{\sigma}{p_w}. \tag{24}$$

Such a definition is reasonable for closed-base gaskets, see the experiments documented in (Shalabi et al., 2016). Notably, $\xi > 1$ refers to a leakproof joint. The larger the value of the safety factor ξ, the smaller the likeliness of leakage. $\xi = 1$ refers to a joint which has reached a groundwater-ingress limit state. $\xi < 1$ holds for a joint at which groundwater ingress is expected. The absolute values of the relative rotations at which a groundwater-ingress limit state is reached are decreasing with increasing groundwater pressure, see Fig. 9.
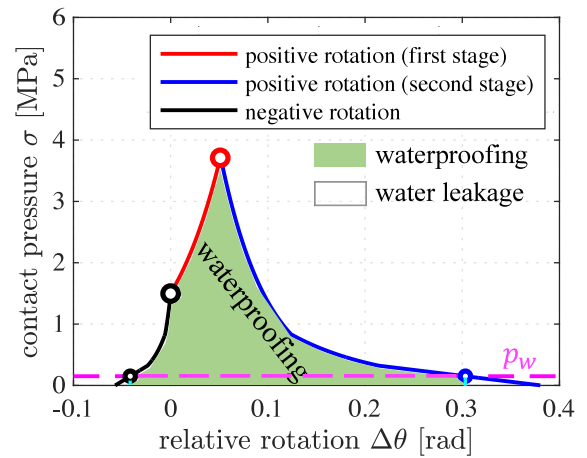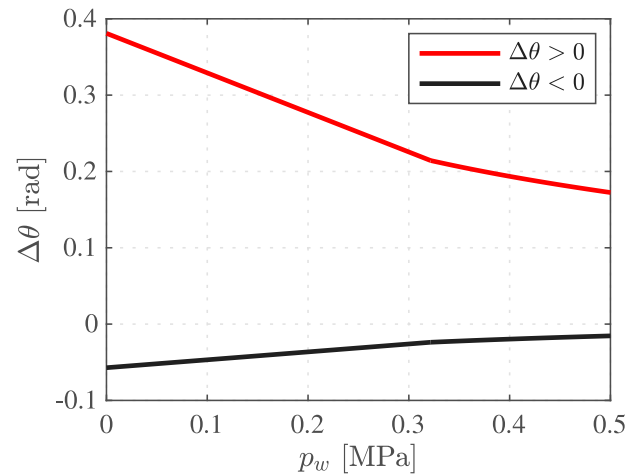
4. Application to the segmental tunnel lining of Metro Line 7 in Shanghai

In the present section, the methods described in Sections 2 and 3 are applied to the segmental tunnel lining of the Metro Line 7 in Shanghai. The tubbing rings have aligned longitudinal joints (see Fig. 10), positioned at angular coordinates given in Eqs. (1). Each longitudinal joint is equipped with one pair of gaskets, as illustrated in Fig. 3(a). The outer diameter of the lining, D_o, amounts to 6.2 m. In the most critical part of the tunnel, the hydraulic head of the groundwater is around 15 m. Thus, the ground groundwater pressure p_w is equal to 0.15 MPa.

The method developed for quantification of a convergence-related safety against water ingress will be applied to convergences increasing from zero, passing three serviceability classes, denoted A, B, and C, up to 124 mm, which is the convergence-related serviceability limit state, see Table 3. Notably, the serviceability classes are based on the larger absolute value of the horizontal and the vertical convergence:

$$C_{max} = \max\{|C_v|, |C_h|\}. \tag{25}$$

Fig. 10. Segmental tunnel lining of Metro Line 7 in Shanghai, consisting of tubbing rings with aligned longitudinal joints; a rail-bound vehicle, equipped with non-metric CCD cameras, was used for inspection of the tunnel by Ai and Yuan (2019).

Table 3
Classification of the convergence-related serviceability according to (T/CSPSTC 43-2019, 2019): C_{max} is defined in Eq. (25), D_o denotes the outer diameter of the segmental tunnel lining (herein: $D_o = 6.2$ m).

class	serviceability	criterion
A	acceptable	$C_{max} \leq 0.8\% D_o$
B	reduced	$0.8\% D_o < C_{max} \leq 1.2\% D_o$
C	endangered	$1.2\% D_o < C_{max} \leq 2\% D_o$
D	violated	$C_{max} > 2\% D_o$

The method summarized in Section 2 allows for quantifying relative rotations at longitudinal joints provided that the horizontal and vertical convergences are known. In the given context it is assumed that the vertical convergences are proportional to the horizontal convergences. This assumption is reasonable because of the following fact. If symmetric tubbing rings undergo symmetric rigid-body displacements, see Fig. 2(a), the absolute value of the vertical convergence, $|C_v|$, is 1.009 times larger than that of the horizontal convergence, $|C_h|$, see (Jiang et al., 2021) for details. Herein, a sensitivity analysis regarding the proportionality factor is performed. 1.009 is used as a first choice for the proportionality of C_v and C_h, for the case of a symmetric mode of rigid-body displacements.

In tunneling practice, however, the absolute value of the vertical convergence is frequently smaller than that of the horizontal convergence: $|C_v/C_h| < 1$. This underlines that the rigid-body displacements of the tubbing rings also include antisymmetric modes (Jiang et al., 2021). Therefore, the sensitivity analysis regarding the proportionality factor between C_v and C_h is associated with the following "asymmetry index":

$$\omega = \frac{1.009 - |C_v/C_h|}{1.009} . \qquad (26)$$

Three values are assigned to this index: $\omega = \{0.00 \ ; \ 0.20 \ ; \ 0.40\}$. Inserting them into Eq. (26) and solving the resulting expressions for $|C_v|$ yields:

$$|C_v| = \lambda \times |C_h|, \qquad \lambda = \{1.0090 \ ; \ 0.8072 \ ; \ 0.6065\} . \qquad (27)$$

4.1. Evolution of the components β_1, β_2, and β_3 of the three modes of rigid-body displacements in consequence of increasing convergences with ratios λ according to Eq. (27)

Three different scenarios of growing rigid-body displacements of the tubbings are investigated in the framework of a sensitivity analysis. Starting from a circular initial arrangement of the tubbings, it is assumed that the horizontal convergence increases monotonously and that the vertical convergence is proportional to it, with proportionality factors λ according to Eq. (27). For all three scenarios and for progressively increasing pairs of values of C_h and C_v the components β_1, β_2,

and β_3 of the three modes of rigid-body displacements are computed, using the method described in Section 2.

Because $|C_v| = 1.0090 \times |C_h|$ refers to symmetric structural behavior, only the component β_1 of the symmetric mode of rigid-body displacements, see Fig. 2(a), increases with increasing convergences, see the blue line in Fig. 11(a). The components of the two antisymmetric modes, see Fig. 2(b) and (c), are equal to zero: $\beta_2 = \beta_3 = 0$, see the red and the black lines in Fig. 11(a).

Both $|C_v| = 0.8072 \times |C_h|$ and $|C_v| = 0.6065 \times |C_h|$ refer to rigid-body displacements consisting of the three modes illustrated in Fig. 2. The symmetric component β_1 increases linearly with increasing convergences, whereby the slope decreases with decreasing proportionality factor between $|C_v|$ and $|C_h|$, see the blue lines in Figs. 11(a)–(c). The antisymmetric components β_2 and β_3 increase nonlinearly with increasing convergences, see the red and black lines in Fig. 11(b) and (c).

4.2. Evolution of the relative rotations at the joints in consequence of increasing convergences with ratios defined in Eq. (27)

The quantified triples of components of rigid-body displacements, β_1, β_2, and β_3, are representative for one specific pair of values of horizontal and vertical convergences. The triples of β-values in Fig. 11 are inserted into Eq. (2) in order to compute corresponding values of the six relative rotations.

As for the symmetric rigid-body displacement associated with $|C_v| = 1.0090 \times |C_h|$, the relative rotations of all joints are increasing linearly with increasing convergences, see Fig. 12(a). Because of symmetry, the relative rotations are equal at both joints in the region of the crown ($j = 1$ and $j = 6$), in the lateral region ($j = 2$ and $j = 5$), and in the region of the invert ($j = 3$ and $j = 4$), see the red, blue, and black lines, respectively, in Fig. 12(a). $\Delta\theta_1$, $\Delta\theta_3$, $\Delta\theta_4$, and $\Delta\theta_6$ are positive, indicating that the joints in the regions of the crown and of the invert open at their inner sides. $\Delta\theta_2$ and $\Delta\theta_5$ are negative, indicating that the lateral joints open at their outer sides, see also Fig. 2(a).

As for $|C_v| = 0.8072 \times |C_h|$ and $|C_v| = 0.6065 \times |C_h|$, the relative rotations increase subproportionally with increasing convergences, see Fig. 12(b) and (c). At each one of the six joints, a specific evolution of the relative rotation is obtained.

4.3. Evolution of the contact pressure between the gaskets in consequence of increasing convergences with ratios defined in Eq. (27)

The computed sextuples of values of relative rotations, $\Delta\theta_1$, $\Delta\theta_2$, $\Delta\theta_3$, $\Delta\theta_4$, $\Delta\theta_5$, and $\Delta\theta_6$, are representative for one specific pair of values of horizontal and vertical convergences. Each $\Delta\theta_j$-value of every sextuple in Fig. 12 is inserted into Eq. (20) in order to compute the corresponding value of the contact pressure between the gaskets.

As for the symmetric rigid-body displacement associated with $|C_v| = 1.0090 \times |C_h|$, the contact pressures between the gaskets of the joints in the crown-region and the invert-region increase with increasing convergences, because of moderately increasing positive relative rotations [= Stage 1 behavior of Fig. 5(a)], see the red and black lines in Fig. 13(a).

The contact pressure between the gaskets of the *lateral* joints, in turn, decreases with increasing convergences, because of increasing negative relative rotations, see the blue line in Fig. 13(a). Once the horizontal convergence has increased to 74 mm, the contact pressure becomes equal to the groundwater pressure. Thus, a groundwater-ingress limit state is reached, see the circle in Fig. 13(a).

As for $|C_v| = 0.8072 \times |C_h|$ and $|C_v| = 0.6065 \times |C_h|$, the contact pressure between the gaskets of joint 6 first increases and then decreases with increasing convergences, because of a monotonously increasing positive relative rotation in Stage 1 [Fig. 5(a)] and Stage 2 [Fig. 5(b)], respectively, see the dashed red lines in Fig. 13(b) and (c). The most significant decrease of the contact pressure is obtained at joints 1 and 5, at which negative relative rotations increase monotonously with
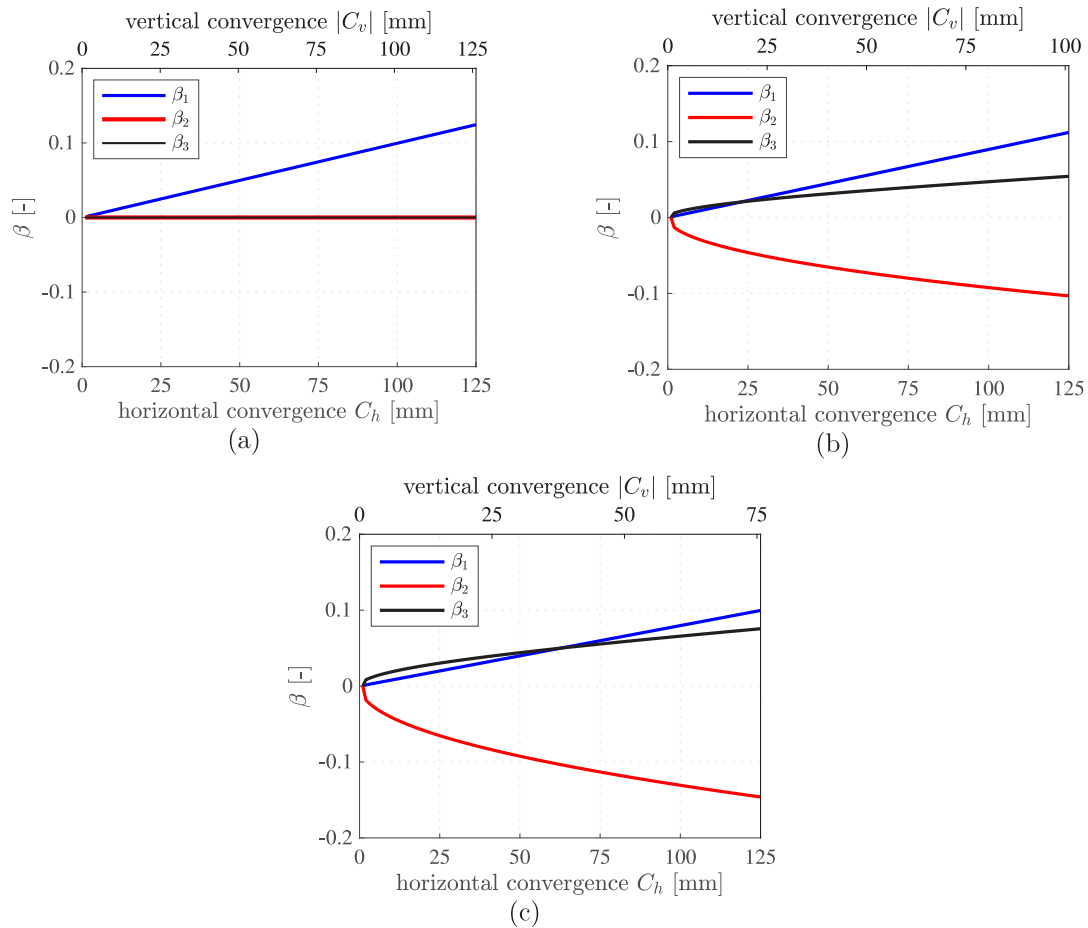
Fig. 11. Evolution of the components β_1, β_2, and β_3 of the three modes of rigid-body displacements illustrated in Fig. 2, resulting from growing convergences with ratios defined in Eq. (27): (a) $|C_v| = 1.0090 \times |C_h|$, (b) $|C_v| = 0.8072 \times |C_h|$, (c) $|C_v| = 0.6065 \times |C_h|$. (For interpretation of the references to color in this figure legend, the reader is referred to the web version of this article.)

increasing convergences. As for moderate asymmetric behavior, $|C_v| = 0.8072 \times |C_h|$, the groundwater-ingress limit state is reached at *lateral* joint 5, once the horizontal convergence has increased to 55 mm, see the circle in Fig. 13(b). As for significant asymmetric behavior, $|C_v| = 0.6065 \times |C_h|$, the groundwater-ingress limit state is reached at *crown* joint 1, once the horizontal convergence has increased to 25 mm, see the circle in Fig. 13(c).

4.4. Evolution of the safety factor against a groundwater-ingress limit state in consequence of increasing convergences with ratios defined in Eq. (27)

The values of the contact pressure in Fig. 13 are inserted, together with $p_w = 0.15$ MPa, into Eq. (24) in order to compute corresponding values of the safety factor against reaching a groundwater-ingress limit state. For each state of convergence, one value of the safety factor ξ is computed for each joint. These values are denoted as ξ_1, ξ_2, ..., ξ_6. A segmental tunnel ring will suffer from ingress of groundwater as soon as the first of the six joints reaches a groundwater-ingress limit state. This provides the motivation for assigning the smallest of these six values to a ring-related safety factor χ:

$$\chi = \min\{\xi_1;\ \xi_2;\ \xi_3;\ \xi_4;\ \xi_5;\ \xi_6\}. \tag{28}$$

$\chi > 1$ refers to a leakproof tunnel ring. The larger the value of the safety factor χ, the smaller the likeliness of leakage. $\chi = 1$ refers to a ring with at least one joint that has reached a groundwater-ingress limit state. $\chi < 1$ refers to a ring through which groundwater ingress is expected to occur.

The ring-related safety factor χ decreases with increasing convergences, see Fig. 14. This decrease is the faster, the larger the deviation from symmetric structural behavior of the tunnel ring (= the smaller the vertical-to-horizontal convergence ratio), see Fig. 14(a). The value of the horizontal convergence, at which a groundwater-ingress limit state is predicted by the model, decreases nonlinearly with increasing deviation from symmetric structural behavior, see Fig. 14(b). The blue line in Fig. 14(b) refers to convergence ratios for which water ingress through one of the lateral joints is predicted, see also Figs. 13(a) and (b), while the red line in Fig. 14(b) refers to convergence ratios for which water ingress through one of joints at the crown is predicted, see also Fig. 13(c).

As for a tunnel underneath the groundwater table, it is intuitive to assume that the distribution of the external pressure acting on the segmental rings is symmetric with respect to a vertical line containing the center of the cross-section considered. It is also intuitive to assume a symmetric deformation of the lining. The corresponding model predictions, see the black line in Fig. 14(a), suggest that all tunnel rings through which water was running into the tunnel of Metro Line 7 in Shanghai, must have had convergences of serviceability class "C: endangered serviceability" or even "D: violated serviceability". This will be checked next, making use of monitored data of the tunnel.

4.5. Model validation based on monitored convergences from Metro 7, in Shanghai

In the most critical part of the tunnel of Metro Line 7 in Shanghai, the convergences have become larger than 2% of the outer diameter,
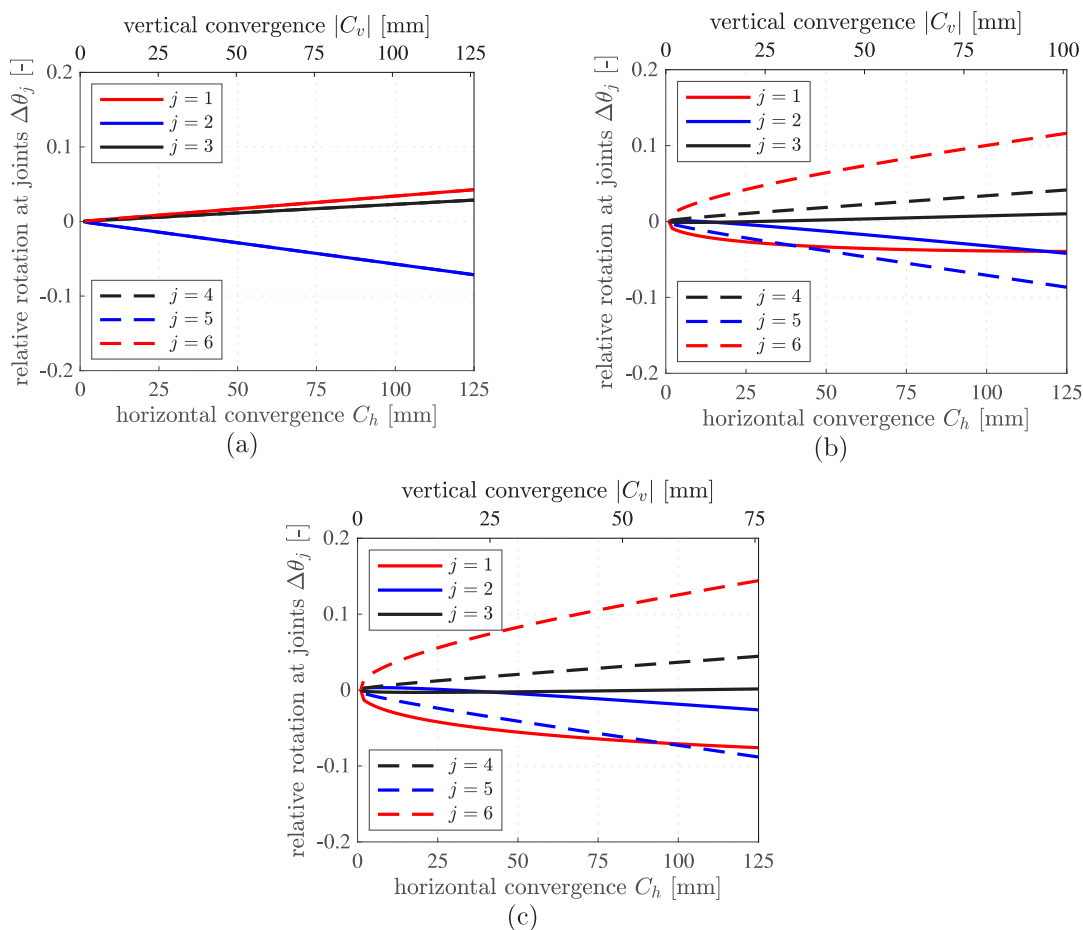
Fig. 12. Evolution of the relative rotations at the six joints, resulting from growing convergences with ratios defined in Eq. (27): (a) $|C_v| = 1.0090 \times |C_h|$, (b) $|C_v| = 0.8072 \times |C_h|$, (c) $|C_v| = 0.6065 \times |C_h|$. (For interpretation of the references to color in this figure legend, the reader is referred to the web version of this article.)

i.e. larger than 124 mm. Thus, the convergence-related serviceability limit state has been surpassed (T/CSPSTC 43-2019, 2019). This part of the tunnel and the immediately adjacent stretches of it were inspected by Ai and Yuan (2019), using a rail-bound vehicle equipped with non-metric CCD cameras, see Fig. 10. Images of the lining were taken while the vehicle was moving through the tunnel. Postprocessing of the images allowed for detection of groundwater ingress as well as for cracking and spalling of concrete and enabled quantification of the horizontal convergences of the individual tunnel rings.

The horizontal convergences of 57 neighboring tubbing rings through which groundwater was running into the tunnel are illustrated in Fig. 15. The convergences of all 57 rings were so large that they had to be assigned to the convergence-related serviceability class "C: endangered serviceability", or even "D: violated serviceability", as predicted by the developed model. This underlines the usefulness of the model.

5. Effect of two pairs of gaskets on groundwater-ingress limit states

Because of the eccentricity of the single pair of gaskets illustrated in Fig. 3(a), its capacity to withstand relative rotations without reaching a groundwater-ingress limit state is significantly smaller for negative than for positive relative rotations, see Figs. 8 and 9. Promising solutions for the improvement of this situation are systems consisting of two pairs of gaskets.

The satisfactory performance of the developed model, demonstrated in Section 4.5, provides the motivation for its application for assessing the effectiveness of placing two sets of gaskets at each longitudinal

joint. Thereby, the focus rests on arrangements of gaskets proposed by Xie et al. (2022) and Ding et al. (2022), see Fig. 16.

Systems consisting of two pairs of gaskets are typically used in large-diameter tunnels (Jin et al., 2017; Feng et al., 2018). Corresponding segments have a height which is frequently larger than 500 mm. Unfortunately, the authors did not have access to monitored convergences of segmental linings where the longitudinal joints are equipped with two pairs of gaskets, and where the convergences have grown so large that water was running into the tunnel. Therefore, continued model validation is out of reach. Still, it is of conceptual interest to use the developed method also for the analysis of systems with two pairs of gaskets per joint. In order to demonstrate the associated benefits relative to the analyzed system with one pair of gaskets per joint, the same tunnel diameter and the same height of the segments will be analyzed in the following.

5.1. Eccentric arrangement of two pairs of gaskets according to Fig. 16(a)

Xie et al. (2022) proposed an eccentric arrangement of two pairs of gaskets. Both pairs are nearer to the outer than to the inner edge of the joint, see Fig. 16(a). Initially, the groundwater is stopped by the outer pair of gaskets. It behaves like the single pair of gaskets described in Section 3, i.e. it very effectively prevents ingress of groundwater in case of a positive relative rotation, while it becomes leaky rather quickly in case of a negative relative rotation. In case of the latter, the inner pair of gaskets takes over, albeit not very effectively. It also becomes leaky rather soon. Because the arrangement of the two pairs of gaskets is still *eccentric*, the relation between the maximum tolerable groundwater
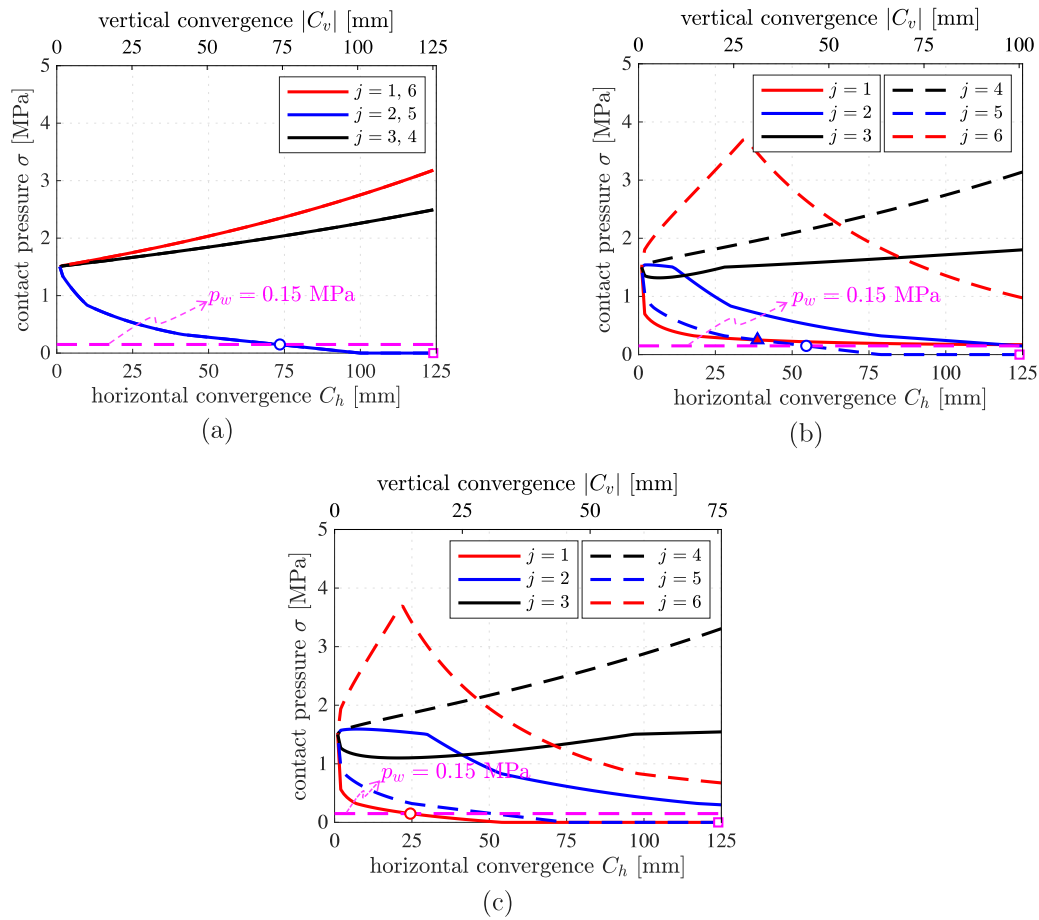
Fig. 13. Evolution of the contact pressure between the gaskets, resulting from growing convergences with ratios defined in Eq. (27): (a) $|C_v| = 1.0090 \times |C_h|$, (b) $|C_v| = 0.8072 \times |C_h|$, (c) $|C_v| = 0.6065 \times |C_h|$. (For interpretation of the references to color in this figure legend, the reader is referred to the web version of this article.)
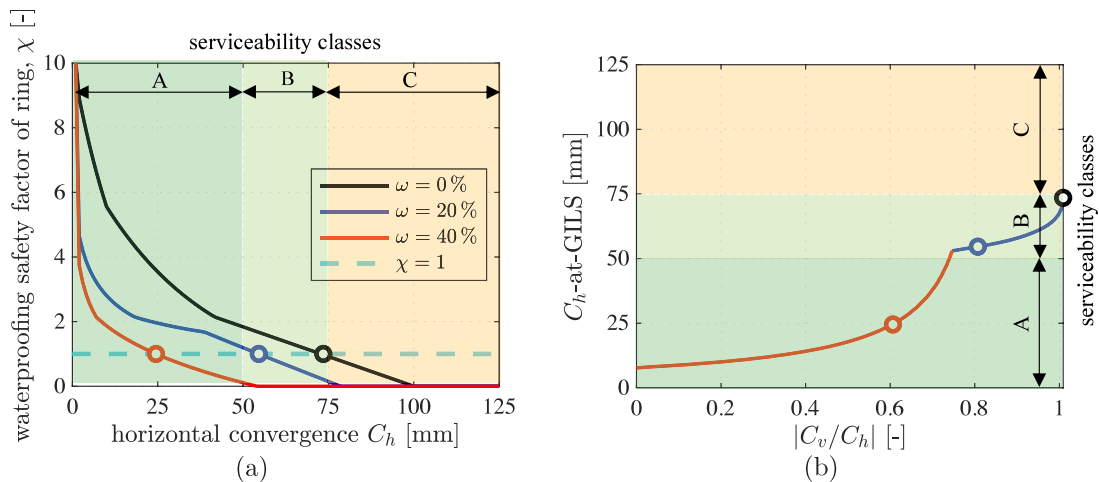

Fig. 14. (a) Evolution of the ring-related safety factor against reaching a groundwater-ingress limit state, χ, resulting from growing convergences with ratios defined in Eq. (27): $|C_v| = 1.0090 \times |C_h|$, see the black line, $|C_v| = 0.8072 \times |C_h|$, see the blue line, and $|C_v| = 0.6065 \times |C_h|$, see the red line, and (b) value of the horizontal convergence at the groundwater-ingress limit state as a function of the vertical-to-horizontal convergence ratio. (For interpretation of the references to color in this figure legend, the reader is referred to the web version of this article.)

pressure, $\max(p_w)$, and the relative rotation at the joint, see the red line in Fig. 17(a), is not significantly better than that of the single pair of gaskets, see the black line in Fig. 17(a).

In order to assess the performance of the eccentric arrangement of two pairs of gaskets, the analysis of the entire tunnel ring, documented in Section 4, is repeated, considering the symmetric mode of the

rigid-body displacements, i.e. for $|C_v| = 1.0090 \times |C_h|$. The maximum admissible groundwater pressure decreases with increasing convergence, see the red line in Fig. 17(b), qualitatively similar to the decrease computed for a single pair of gaskets, see the black line in Fig. 17(b). Still, the performance of two pairs of gaskets is quantitatively better. As for a groundwater pressure amounting to 0.15 MPa, the analysis
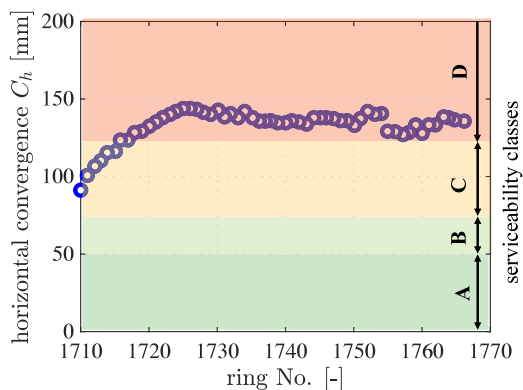
Fig. 15. Horizontal convergences of 57 tubbing rings (with numbers running from 1710 to 1766) of the segmental tunnel lining of Metro Line 7 in Shanghai, through which water was running into the tunnel, as detected by Ai and Yuan (2019) by means of photos taken by non-metric CCD cameras, see Fig. 10.

suggests that the single pair of gaskets becomes leaky at the border of convergence-related serviceability classes B and C, while the eccentric arrangement of two pairs of gaskets becomes leaky close to the center of convergence-related serviceability class C at a convergence which is by 35% larger than that at the border of the classes B and C, see Fig. 17(b).

5.2. Symmetric arrangement of two pairs of gaskets according to Fig. 16(b)

Ding et al. (2022) proposed a symmetric arrangement of two pairs of gaskets. One pair is near to the outer edge of the joint and the other one near to the inner edge, see Fig. 16(b). Initially, the groundwater is stopped by the outer pair of gaskets. It behaves like the single pair of gaskets, as described in Section 3, i.e. it very effectively prevents ingress of groundwater in case of a positive relative rotation, while failing rather soon in case of a negative relative rotation. In case of the latter, however, the inner pair of gaskets takes over and very effectively prevents ingress of groundwater. Because of the *symmetric* arrangement of the gaskets, the largest tolerable groundwater pressure, $\max(p_w)$, is the same for positive *and* negative relative rotations, see the blue graph in Fig. 17(a). Note its symmetry with respect to $\Delta\theta = 0$.

In order to assess the performance of the symmetric arrangement of two pairs of gaskets, the analysis of an entire tunnel ring of Section 4 is repeated, considering the symmetric mode of the rigid-body displacements, i.e. for $|C_v| = 1.0090 \times |C_h|$. The maximum admissible groundwater pressure even increases with increasing convergence all the way up to the end of convergence-related serviceability class C, see Fig. 17(b). In the convergence-related serviceability class D, the maximum tolerable groundwater pressure decreases. When the horizontal convergence becomes equal to 3% of the initial outer diameter of the tunnel ring, the remaining maximum tolerable groundwater pressure still amounts to 88% of the initial contact pressure between the gaskets, see Fig. 17(b). Therefore, the symmetric arrangement of two pairs of gaskets is very effective, ensuring that tunnel rings remain leakproof. This requires, however, that the channels, hosting the bolts that connect neighboring tubbings, are suitably sealed (Ding et al., 2022). This is a challenging task which is beyond the scope of the present paper.

6. Summary and conclusions

The presented approach was developed for prediction of groundwater-ingress limit states of segmental tunnel rings, using measured convergences as input. It is a multiscale approach, starting at the scale of observation of an entire tunnel ring, progressing to that of the joints, and ending at that of the gaskets:

- Measured convergences are transformed to values of the relative rotations at the joints. This is achieved by means of a kinematic analysis of the entire tunnel ring (Zhang et al., 2022a), based on the assumption that rigid-body displacements of the tubbings govern the convergences.
- The relative rotations are converted to changes of the shortening of the gaskets. This is accomplished by means of a local kinematic analysis of each joint, again based on the assumption that tubbings behave like rigid bodies.
- Changes of the shortening of the gaskets are translated into corresponding changes of their contact pressure. This step of the analysis is based on results from direct compression tests performed on one pair of gaskets by Shen (2012).
- A comparison of the contact pressure between two gaskets with the groundwater pressure allows for assessing whether or not the investigated pair of gaskets reaches a groundwater-ingress limit state.

The described approach was applied to the segmental lining of Metro Line 7 in Shanghai. From the obtained results the following conclusions can be drawn:

- The values of the convergences, suggested by the developed approach to mark the groundwater-ingress limit state, are smaller than the convergences of the 57 rings of Metro Line 7 in Shanghai, characterized by groundwater ingress into the tunnel. Thus, the model delivers conservative estimates of groundwater-ingress limit states (= estimates on the safe side). In the given case, this is considered as advantageous.
- As for symmetric deformations of tunnel rings, groundwater runs through the *lateral* joints into the tunnel, because they are subjected to negative relative rotations. This goes along with an opening close to groundmass-side of the joints. The pair of gaskets, positioned eccentrically near to the outer edges of the joints, soon becomes leaky.
- With increasing asymmetry of the deformations of tunnel rings, the convergence associated with a groundwater-ingress limit state decreases. The first joints which become leaky change from the lateral region to the crown.

From the analysis of systems consisting of two pairs of gaskets, the following conclusions can be drawn:

- The *eccentric* arrangement of two pairs of gaskets, proposed by Xie et al. (2022), increases the groundwater-ingress-related convergence by 35%, compared to the traditional arrangement of one pair of eccentric gaskets. In other words, the groundwater-ingress-related convergence is shifted from the boundary between convergence-related serviceability classes B and C to the center of convergence-related serviceability class C, see Fig. 17(b).
- The *symmetric* arrangement of two pairs of gaskets proposed by Ding et al. (2022) ensures that the convergence-related serviceability is violated before a groundwater-ingress limit state is reached. Still, this approach requires sealing of the channel of the bolts which is difficult to achieve.

Finally, the limitations of the study are addressed. The presented approach is limited to tunnel rings with insignificant ring-to-ring interaction. This is a necessary condition for the validity of the underlying assumption that rigid-body displacements of the tubbings govern the convergences. Notably, ring-to-ring interaction is frequently insignificant in segmental linings with *aligned* longitudinal joints, as were installed in the tunnel of the investigated Metro Line 7, in Shanghai. Furthermore, validation of the presented approach is limited to linings with *one pair of gaskets* per longitudinal joint. Unfortunately, the authors did not have access to monitored convergences of segmental linings where the longitudinal joints are equipped with two pairs of
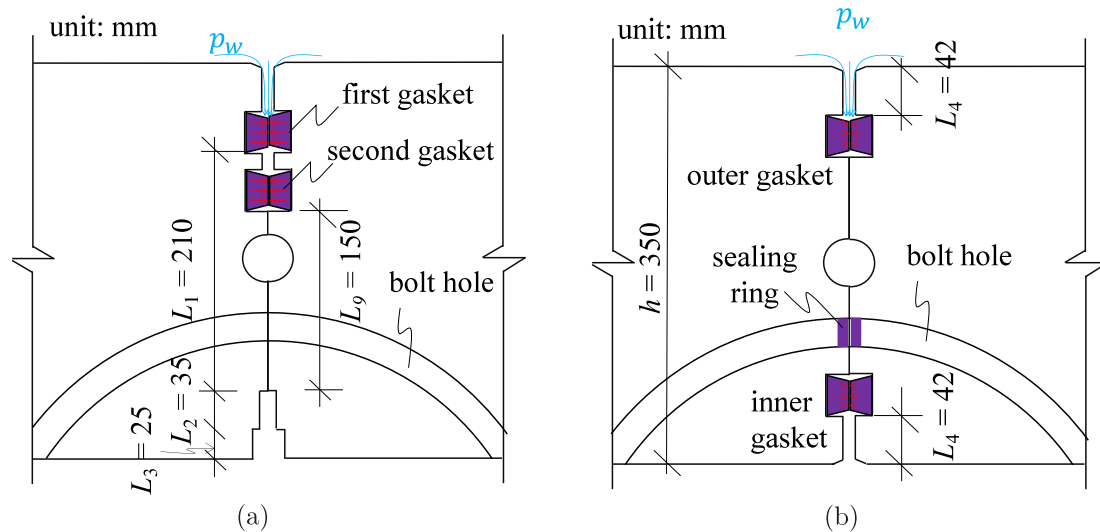
Fig. 16. Systems consisting of two pairs of gaskets: (a) eccentric arrangement of two pairs of gaskets according to (Xie et al., 2022), with both pairs of gaskets nearer to the outer edge, and (b) symmetric arrangement of two pairs of gaskets according to (Ding et al., 2022), with one pair nearer to the inner edge of the joint and the other one nearer to the outer edge.
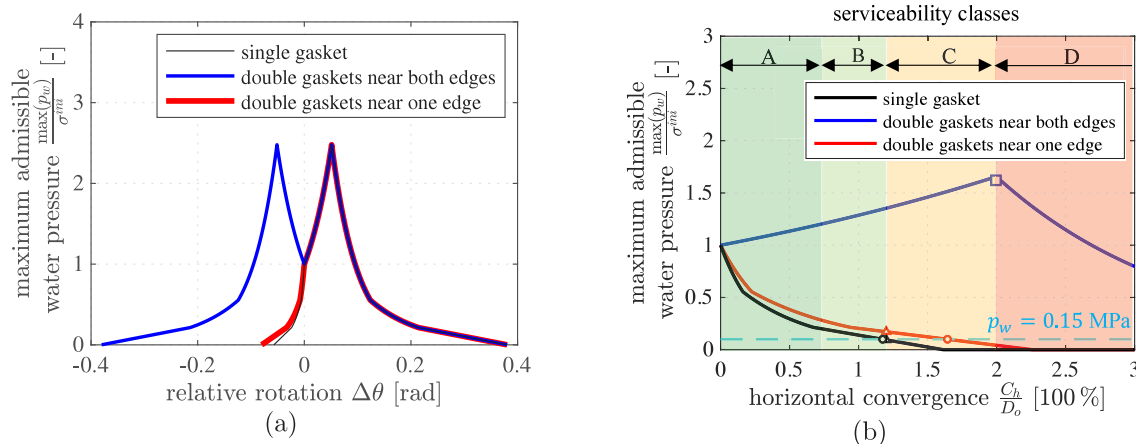

Fig. 17. Influence of the arrangement of one and two pairs, respectively, of gaskets on groundwater-ingress limit states of (a) individual joints, and (b) entire segmental tunnel rings. (For interpretation of the references to color in this figure legend, the reader is referred to the web version of this article.)

gaskets, and where the convergences have grown so large that water was running into the tunnel. Nonetheless, such cases were also analyzed for illustration purposes. Their validation leaves space for future research work.

CRediT authorship contribution statement

Jiao-Long Zhang: Conceptualization, Methodology, Software, Writing – original draft. **Yong Yuan:** Supervision, Funding acquisition. **Xian Liu:** Data curation, Investigation. **Herbert A. Mang:** Writing – review & editing. **Bernhard L.A. Pichler:** Conceptualization, Supervision, Writing – review & editing.

Declaration of competing interest

The authors declare that they have no known competing financial interests or personal relationships that could have appeared to influence the work reported in this paper.

Data availability

Data will be made available on request.

Appendix A. Derivation of conditions for relative rotation angles at the joints, resulting in rigid-body displacements of segments

Assuming that the convergences of segmental linings are governed by rigid-body displacements of the tubbings, relative rotations at the joints connecting neighboring tubbings can be estimated by means of known values of horizontal and vertical convergences (Zhang et al.,

2022a). Essential fundamentals of this statement will be briefly recalled in the following. The focus is on segmental rings consisting of six tubbings, as are used for the linings of metro tunnels in Shanghai, see Fig. 1(a).

Rigid-body displacements of the tubbings can be described by means of a set of functions of the relative rotations at the joints, $\Delta\theta_j$ with $j = 1, 2, \ldots, 6$, reading as (Zhang et al., 2017, 2019a,b, 2021)

$$u(\varphi) = \sum_{j=1}^{6} R\Delta\theta_j \sin(\varphi - \varphi_j) H(\varphi - \varphi_j), \tag{A.1}$$

$$v(\varphi) = -\sum_{j=1}^{6} R\Delta\theta_j \left[1 - \cos(\varphi - \varphi_j)\right] H(\varphi - \varphi_j), \tag{A.2}$$

$$\theta(\varphi) = \sum_{j=1}^{6} \Delta\theta_j H(\varphi - \varphi_j), \tag{A.3}$$

where u, v, and θ denote the radial displacement, the tangential displacement, and the cross-sectional rotation, respectively, and $H(x)$ stands for the Heaviside step function which is equal to 1 for $x > 1$ and to 0 otherwise.

Considering the continuity conditions of a closed segmental tunnel ring delivers the following three equations for the six relative rotations (Zhang et al., 2019a; Jiang et al., 2021):

$$u(0) = u(2\pi) \Rightarrow \sum_{j=1}^{6} \Delta\theta_j \sin\varphi_j = 0, \tag{A.4}$$

$$v(0) = v(2\pi) \Rightarrow \sum_{j=1}^{6} \Delta\theta_j (1 - \cos\varphi_j) = 0, \tag{A.5}$$

$$\theta(0) = \theta(2\pi) \Rightarrow \sum_{j=1}^{6} \Delta\theta_j = 0. \tag{A.6}$$

Appendix B. Fitting formulae for the lines in Fig. 14

Herein, fitting formulae for approximating the waterproofing safety factor of the tunnel rings, χ, as a function of horizontal convergence, C_h, and the horizontal convergence at the groundwater-ingress limit state as a function of the vertical-to-horizontal convergence ratio, λ, are provided. In case of $|C_v| = 1.0090 \times |C_h|$, see the black line in Fig. B.1(a), the fitting formula for χ reads as

$$\chi = \begin{cases} -2.931\,(C_h)^{0.3171} + 11.68 \ldots. & 10\,\text{mm} \le C_h < 42\,\text{mm}, \\ -0.0368\,C_h + 3.676 \ldots\ldots\ldots & 42\,\text{mm} \le C_h \le 100\,\text{mm}, \\ 0 \ldots\ldots\ldots\ldots\ldots\ldots\ldots & 100\,\text{mm} \le C_h. \end{cases} \tag{B.1}$$

In case of $|C_v| = 0.8072 \times |C_h|$, see the blue line in Fig. B.1(a), the fitting formula for χ reads as

$$\chi = \begin{cases} 6.252\,(C_h)^{-0.3583} \ldots\ldots & 2\,\text{mm} \le C_h < 39\,\text{mm}, \\ -0.0420\,C_h + 3.293 \ldots & 39\,\text{mm} \le C_h \le 79\,\text{mm}, \\ 0 \ldots\ldots\ldots\ldots\ldots & 79\,\text{mm} \le C_h. \end{cases} \tag{B.2}$$

In case of $|C_v| = 0.6065 \times |C_h|$, see the red line in Fig. B.1(a), the fitting formula for χ reads as

$$\chi = \begin{cases} -20.48\,(C_h)^{0.0466} + 24.73; \ldots & 2\,\text{mm} \le C_h < 55\,\text{mm}, \\ 0 \ldots\ldots\ldots\ldots\ldots\ldots & 55\,\text{mm} \le C_h. \end{cases} \tag{B.3}$$

Fitting function for the horizontal convergence at the groundwater-ingress limit state with respect to the vertical-to-horizontal convergence ratio λ, see Fig. B.1(b), reads as

$$C_h = \begin{cases} 7.159\,e^{1.725\,\lambda} + 1.151 \times 10^{-3}\,e^{13.46\,\lambda} & 0.7470 \le \lambda = |C_v/C_h| \le 1.009, \\ 37.37\,e^{0.4737\,\lambda} + 3.73 \times 10^{-14}\,e^{33.11\,\lambda} \ldots & 0 \le \lambda = |C_v/C_h| < 0.7470. \end{cases} \tag{B.4}$$

Appendix C. List of symbols

|	
$\boldsymbol{A}$	matrix containing base vectors of relative rotations at the joints
$A_{i,j}$	element of $\boldsymbol{A}$
C	model-predicted convergence
C^{mea}	measured convergence
C_h	horizontal convergence
C_{max}	larger one of the absolute values of the horizontal and the vertical convergence
C_v	vertical convergence
D_o	outer diameter of the tunnel ring
d_2 and d_3	constants related to k_1, k_2, and k_3
H	Heaviside function
h	radial thickness of the tubbings
$L_{i=1,2,\ldots,9}$	numerical values of the geometric dimensions labeled in Figs. 3(a), 5, 6, and 16
l_i	height of the gaskets without any compression
l_0	height of precompressed gaskets in the initial configuration of the circular tunnel ring
$k_{1,2,3}$	calibration parameters for the relation between the contact pressure and the shortening of the gaskets
p_w	external groundwater pressure
R	radius of the axis of the segmental tunnel ring
RMS	root mean square error between measured and modeled convergences
u	radial component of the displacement
v	circumferential component of the displacement
$\boldsymbol{\beta}$	vector, containing components associated with the base vectors of fundamental solutions for relative rotations at the joints
β_1	component associated with the symmetric mode of rigid-body displacements
β_1^{opt}	optimal value of β_1
β_2	component associated with the first antisymmetric mode of rigid-body displacements
β_2^{opt}	optimal value of β_2
β_3	component associated with the second antisymmetric mode of rigid-body displacements
β_3^{opt}	optimal value of β_3
$\Delta\theta_j$	relative rotation at the jth joint
Δl	shortening of the gaskets
Δl_{t1} and Δl_{t2}	interval boundaries for the three different intervals of Δl
Δl_1	shortening of the gaskets in Stage 1 of the relative rotation
Δl_2	shortening of the gaskets in Stage 2 of the relative rotation
$\Delta l_{1\to2}$	transition shortening of the gaskets from Stage 1 to Stage 2 of the relative rotation
$\Delta\theta$	vector of relative rotations at the joints
$\Delta\theta_{1\to2}$	transition relative-rotation at the joints from its Stage 1 to Stage 2
$\Delta\theta_{n1,n2,n3}$	interval boundaries for negative relative rotations
$\Delta\theta_{p1,p2,p3,p4}$	interval boundaries for positive relative rotations
σ	contact pressure between the paired gaskets
θ	cross-sectional rotation angle
φ	angular coordinate of the polar coordinate system
φ_j	polar position of the jth joint of the segmental tunnel ring
ψ	angular coordinate of the polar coordinate system
ψ_k	k^{th} direction in which the convergence is measured
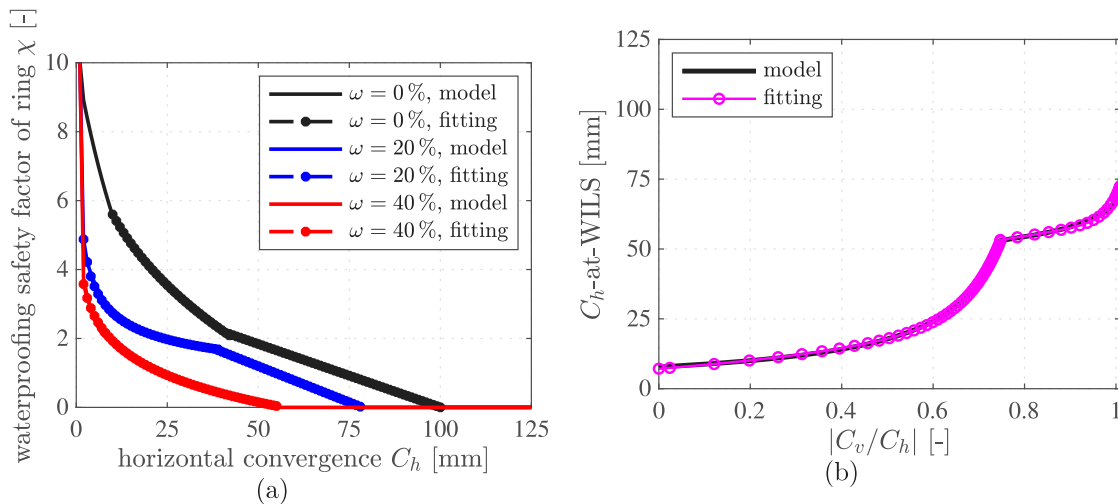
Fig. B.1. (a) Fitting of the function of the ring-related safety factor against reaching a groundwater-ingress limit state, χ, with respect to the horizontal convergences, and (b) fitting of the function of the horizontal convergence at the groundwater-ingress limit state with respect to the vertical-to-horizontal convergence ratio.

δ_{jk}	Kronecker delta
λ	proportionality factor between absolute values of the vertical and the horizontal convergence
φ_j	relative rotation angle of the jth joint of segmental tunnel rings
Δl_{ini}	initial shortening of the gaskets
φ	angular coordinate
ω	asymmetry index
ξ	joint-related factor quantifying the safety against groundwater ingress
χ	ring-related factor quantifying the safety against groundwater ingress

References

Ai, Q., Yuan, Y., 2019. Rapid acquisition and identification of structural defects of metro tunnel. Sensors 19 (19), 4278.

Ai, Q., Yuan, Y., Bi, X., 2016. Acquiring sectional profile of metro tunnels using charge-coupled device cameras. Struct. Infrastruct. Eng. 12 (9), 1065–1075.

Attard, L., Debono, C.J., Valentino, G., Di Castro, M., 2018. Tunnel inspection using photogrammetric techniques and image processing: A review. ISPRS J. Photogramm. Remote Sens. 144, 180–188.

Blom, C., 2002. Design Philosophy of Concrete Linings for Tunnels in Soft Soils (Ph.D. thesis). Delft University of Technology, The Netherlands.

Cui, H., Ren, X., Mao, Q., Hu, Q., Wang, W., 2019. Shield subway tunnel deformation detection based on mobile laser scanning. Autom. Constr. 106, 102889.

DG/TJ08-2123-2013, 2013. Code for Structural Appraisal of Shield Tunnel. Tech. Rep., Shanghai Municipal Commission of City Development and Transport, Shanghai, In Chinese.

Ding, W., Wang, Q., Qiao, Y., Jin, Y., 2022. Experimental investigation on waterproofing performance of segmental joint with double gaskets for shield tunnel. Undergr. Space 7 (5), 898–910.

El Naggar, H., Hinchberger, S., 2008. An analytical solution for jointed tunnel linings in elastic soil or rock. Can. Geotech. J. 45 (11), 1572–1593.

Feng, K., He, C., Qiu, Y., Zhang, L., Wang, W., Xie, H., Zhang, Y., Cao, S., 2018. Full-scale tests on bending behavior of segmental joints for large underwater shield tunnels. Tunn. Undergr. Space Technol. 75, 100–116.

Gong, C., Ding, W., Soga, K., Mosalam, K.M., 2019. Failure mechanism of joint waterproofing in precast segmental tunnel linings. Tunn. Undergr. Space Technol. 84, 334–352.

Gong, C., Wang, Y., Ding, W., Lei, M., Shi, C., 2022. Waterproof performance of sealing gasket in shield tunnel: A review. Appl. Sci. 12 (9), 4556.

Huang, H., Cheng, W., Zhou, M., Chen, J., Zhao, S., 2020. Towards automated 3D inspection of water leakages in shield tunnel linings using mobile laser scanning data. Sensors 20 (22), 6669.

Huang, Z., Fu, H.-L., Fan, X.-D., Meng, J.-H., Chen, W., Zheng, X.-J., Wang, F., Zhang, J.-B., 2021. Rapid surface damage detection equipment for subway tunnels based on machine vision system. J. Infrastruct. Syst. 27 (1), 04020047.

Huang, H.-W., Li, Q.-T., Zhang, D.-M., 2018. Deep learning based image recognition for crack and leakage defects of metro shield tunnel. Tunn. Undergr. Space Technol. 77, 166–176.

Huang, H., Shao, H., Zhang, D., Wang, F., 2017. Deformational responses of operated shield tunnel to extreme surcharge: A case study. Struct. Infrastruct. Eng. 13 (3), 345–360.

Jiang, Z., Liu, X., Schlappal, T., Zhang, J.-L., Mang, H.A., Pichler, B.L., 2021. Asymmetric serviceability limit states of symmetrically loaded segmental tunnel rings: Hybrid analysis of real-scale tests. Tunn. Undergr. Space Technol. 113, 103832.

Jin, Y., Ding, W., Yan, Z., Soga, K., Li, Z., 2017. Experimental investigation of the nonlinear behavior of segmental joints in a water-conveyance tunnel. Tunn. Undergr. Space Technol. 68, 153–166.

Li, X., Lin, X., Zhu, H., Wang, X., Liu, Z., 2017. Condition assessment of shield tunnel using a new indicator: The tunnel serviceability index. Tunn. Undergr. Space Technol. 67, 98–106.

Meng, X., Wu, W., Zhu, H., Jiao, Y., Jin, R., Tu, X., 2023. Gas sealing behavior of gasketed segmental joints in shield tunnels: An experimental and computational study. Tunn. Undergr. Space Technol. 132, 104906.

Nuttens, T., Stal, C., De Backer, H., Schotte, K., Van Bogaert, P., De Wulf, A., 2014. Methodology for the ovalization monitoring of newly built circular train tunnels based on laser scanning: Liefkenshoek rail link (Belgium). Autom. Construct. 43, 1–9.

Shalabi, F.I., Cording, E.J., Paul, S.L., 2016. Sealant behavior of gasketed segmental tunnel lining–conceptual model. Geomech. Tunn. 9 (4), 345–355.

Shen, B.-W., 2012. Research on Joint Interface of Soft Soil Shield Tunnel Lining (Master's thesis). Tongji University, Shanghai China, In Chinese.

T/CSPSTC 43-2019, 2019. Technical Specification for Health Monitoring of Metro Underground Structure. Tech. Rep., China Society for the Promotion of Science and Technology Commercialization, Beijing, In Chinese.

Walton, G., Delaloye, D., Diederichs, M.S., 2014. Development of an elliptical fitting algorithm to improve change detection capabilities with applications for deformation monitoring in circular tunnels and shafts. Tunn. Undergr. Space Technol. 43, 336–349.

Wu, H.-N., Huang, R.-Q., Sun, W.-J., Shen, S.-L., Xu, Y.-S., Liu, Y.-B., Du, S.-J., 2014. Leaking behavior of shield tunnels under the Huangpu River of Shanghai with induced hazards. Nat. Hazards 70 (2), 1115–1132.

Xie, X., Lu, X., 2017. Development of a 3D modeling algorithm for tunnel deformation monitoring based on terrestrial laser scanning. Undergr. Space 2 (1), 16–29.

Xie, H., Wang, S., He, C., Ma, T., Peng, X., Li, P., 2022. Performance of a new waterproof system with double sealing gaskets outside bolt hole of segment. Tunn. Undergr. Space Technol. 119, 104206.

Xu, J., Ding, L., Luo, H., Chen, E.J., Wei, L., 2019. Near real-time circular tunnel shield segment assembly quality inspection using point cloud data: A case study. Tunn. Undergr. Space Technol. 91, 102998.

Xu, L., Gong, J., Na, J., Yang, Y., Tan, Z., Pfeifer, N., Zheng, S., 2022. Shield tunnel convergence diameter detection based on self-driven mobile laser scanning. Remote Sens. 14 (3), 767.

Yi, C., Lu, D., Xie, Q., Liu, S., Li, H., Wei, M., Wang, J., 2019. Hierarchical tunnel modeling from 3D raw LiDAR point cloud. Comput. Aided Des. 114, 143–154.

Yuan, Y., Bai, Y., Liu, J., 2012. Assessment service state of tunnel structure. Tunn. Undergr. Space Technol. 27 (1), 72–85.

Zhang, J.-L., Jiang, Z., Liu, X., Yuan, Y., Mang, H.A., Pichler, B., 2022a. Identification of deformed configurations of segmental tunnel rings based on measured convergences. Tunn. Undergr. Space Technol. 135, 105033.

Zhang, D.-M., Liu, J., Huang, Z.-K., Yang, G.-H., Jiang, Y., Jia, K., 2022b. Waterproof performance of tunnel segmental joints under different deformation conditions. Tunn. Undergr. Space Technol. 123, 104437.

Zhang, J.-L., Liu, X., Yuan, Y., Mang, H.A., Pichler, B.L., 2021. Transfer relations: Useful basis for computer-aided engineering of circular arch structures. Eng. Comput. 38 (3), 1287–1302.

Zhang, J.-L., Mang, H., Liu, X., Yuan, Y., Pichler, B., 2019a. On a nonlinear hybrid method for multiscale analysis of a bearing-capacity test of a real-scale segmental tunnel ring. Int. J. Numer. Anal. Methods Geomech. 43 (7), 1343–1372.

Zhang, J.-L., Schlappal, T., Yuan, Y., Mang, H.A., Pichler, B., 2019b. The influence of interfacial joints on the structural behavior of segmental tunnel rings subjected to ground pressure. Tunn. Undergr. Space Technol. 84, 538–556.

Zhang, J.L., Vida, C., Yuan, Y., Hellmich, C., Mang, H., Pichler, B., 2017. A hybrid analysis method for displacement-monitored segmented circular tunnel rings. Eng. Struct. 148, 839–856.